

Article

Effects of Oxygen Content on Microstructure and Creep Property of Powder Metallurgy Superalloy

Yufeng Liu ^{1,*}, Shaorong Zhang ², Lichong Zhang ¹, Liang Zheng ¹, Zhou Li ¹, Lin Zhang ² and Guoqing Zhang ¹

¹ Science and Technology on Advanced High Temperature Structural Materials Laboratory, AECC Beijing Institute of Aeronautical Materials, Beijing 100095, China

² Beijing Advanced Innovation Center for Materials Genome Engineering, Institute for Advanced Materials and Technology, University of Science and Technology Beijing, Beijing 100083, China

* Correspondence: yufeng.liu@biam.ac.cn

Abstract: The effects of oxygen content on the microstructure and creep properties of the FGH96 superalloy were investigated. When oxygen content increased from 135 ppm to 341 ppm, the prior particle boundary (PPB) rose from degree 2 to degree 3, the size of the γ' phase on PPB enlarged from 1.07 μm to 1.27 μm , and the MC carbide size grew from 77.4 nm to 104.0 nm. Meanwhile, the steady creep rate accelerated from $4.34 \times 10^{-3} \text{ h}^{-1}$ to $1.87 \times 10^{-2} \text{ h}^{-1}$, and the creep rupture life shortened from 176 h to 94 h, the creep rupture mode transferred from intergranular and transgranular mixed fracture to along PPB fracture. During creep, the micro-twin formation and gliding will be restrained by $\Sigma 3$ boundaries. FGH96 superalloy with higher oxygen content contains less $\Sigma 3$ boundaries, and its micro-twins cross-slipped instead of single-direction slip in lower oxygen content superalloy. Consequently, samples with a higher oxygen content creep faster and ruptured earlier.

Keywords: powder metallurgy superalloy; oxygen content; prior particle boundary; creep



Citation: Liu, Y.; Zhang, S.; Zhang, L.; Zheng, L.; Li, Z.; Zhang, L.; Zhang, G. Effects of Oxygen Content on Microstructure and Creep Property of Powder Metallurgy Superalloy. *Crystals* **2024**, *14*, 358. <https://doi.org/10.3390/cryst14040358>

Academic Editor: Tomasz Sadowski

Received: 16 March 2024

Revised: 29 March 2024

Accepted: 8 April 2024

Published: 10 April 2024



Copyright: © 2024 by the authors. Licensee MDPI, Basel, Switzerland. This article is an open access article distributed under the terms and conditions of the Creative Commons Attribution (CC BY) license (<https://creativecommons.org/licenses/by/4.0/>).

1. Introduction

Powder metallurgy (PM) nickel-based superalloy is widely used on turbine discs and compressor discs of high-performance aero engines due to its fine grain size, uniform microstructure and excellent high-temperature mechanical properties [1,2]. Hot isostatic pressing (HIPing) can completely densify the alloy powder, which is the key for the powder metallurgy process to be applied to the preparation of rotating parts [3,4]. However, Prior Particle Boundary (PPB) easily forms during HIPing, consisting of carbide, oxide, carbon oxide and γ' phase, continuously or semi-continuously distributing along the boundary of the original powder particles [5,6]. Oxygen element adsorbed on the powder particle surface is considered to be the key for the formation of PPB since Ti, Al, Zr and other alloy elements of the nickel-based superalloy are easily able to react with the oxygen element and form stable oxides [7,8]. During HIPing, some of these oxides serve as nucleation and promote the precipitation of PPB [9,10].

The higher the oxygen content of the powder, the more PPB there will be, which deteriorates the microstructure integrity and mechanical properties. Rao et al. [11] studied the effect of oxygen content on the microstructure and mechanical properties of the HIPed Inconel718 alloy and found that PPB especially existed in alloys with high oxygen content. The increase in oxygen content inhibited the formation of recrystallization and annealing twins, which would sharply impair the high-temperature plasticity and fracture toughness, although it had little effect on the yield strength and tensile strength. He et al. [12] studied the effect of the powder-making process on the microstructure and thermal deformation behavior of PM nickel-based superalloy. Results show that, compared with the plasma rotating electrode method, the powder prepared by argon gas atomization formed more PPB at HIPing due to its higher oxygen content and was more likely to crack during subsequent thermal deformation. MacDonald et al. [13] studied the effect of powder

characteristics on the microstructure and mechanical properties of HIPed CM247LC nickel-based superalloy and found that the alloy prepared by coarse powder had lower oxygen content and more $\Sigma 3$ grain boundary, which improved the high temperature properties.

Nevertheless, there are few relevant studies on the influence of oxygen content on the creep properties of PM nickel-based superalloys. Creep performance is an important factor for structural design and life evaluation in aeroengines [14,15]. Therefore, it is necessary to study the effect of oxygen content on the microstructure and creep properties of PM nickel-based superalloys.

2. Materials and Methods

2.1. Alloys and Preparation

The FGH96 superalloy studied in this paper is suitable for the fabrication of the turbine disc operating at temperatures below 750 °C. The prealloying powder was obtained by vacuum induction melting argon gas atomization (VIGA) and sieved into less than 63 μm . For comparison, part of the powder was preoxidized by a heating furnace at 200 °C for 5 h, simulating the heating process that may occur for the high-frequency vibration during sieving in industrial production.

The original and preoxidized FGH96 superalloy powder, approximately 21 kg, were respectively loaded in a stainless-steel bucket with 160 mm in diameter and 200 mm in height. Then, degassing was carried out at 450 °C under pressure below 1.0×10^{-3} Pa for 8 h, followed by encapsulating to prevent air from flowing to these buckets. Finally, the two buckets were HIPed at 1170 °C under 140 MPa for 4 h to obtain a fully densified superalloy with two different oxygen contents.

2.2. Materials Characterization

The oxygen content of the powder and HIPed FGH96 superalloy was detected by the pulse heating-infrared absorption method with an oxygen and nitrogen analyzer (TC600, LECO, San Jose, CA, USA). To ensure the accuracy of the analysis, five samples of each state were obtained. To be specific, powder samples were obtained every 4 kg of loading, while the HIPed samples were machined at five different sites of the densified superalloy, as illustrated in Figure 1. Each sample was tested twice, and the results are displayed in Table 1.

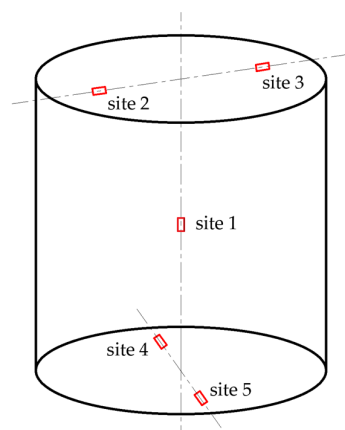


Figure 1. Schematic diagram of the five sampling sites of the densified superalloy.

Table 1. Oxygen content of superalloy under different state (ppm).

State	Original		Preoxidized	
	Average	Standard Deviation	Average	Standard Deviation
Powder	141	13	397	9
HIPed	135	6	341	6

To investigate the effect of oxygen content on the microstructure of the FGH96 superalloy, the samples were ground and mechanically polished for PPB evaluation. For EBSD analysis, these polished samples should be electro-polished a step further in a solution composed of 20 mL HCl + 80 mL CH₃OH under a voltage of 25 V for 15 s. For phase observation by SEM, these electro-polished samples should be electro-etched in a 170 mL H₃PO₄ + 10 mL H₂SO₄ + 15 g CrO₃ solution under a voltage of 5 V for 2–3 s. The PPB degree was estimated with metallographic microscopy (OM, DM8000M, LEICA, Wetzlar, Germany). The γ' phase and carbon morphology were captured using the field emission scanning electron microscope (FE-SEM, Regulus8100, HITACHI, Tokyo, Japan) under back scattering electron mode (BSE). Crystal orientation images, grain size and grain boundary distributions were obtained by electron back scattering diffraction mode (EBSD). The average size and proportion of the γ' phase and carbon were measured by Image-Pro Plus version 6.0 analysis software. Above 1000 grains of each sample were calculated to obtain the average size, and the proportion of γ' phase and carbon were counted from about one square centimeter area. The phase crystal structure and annealing twin were analyzed with a field emission transmission electron microscope (TEM, Tecnai G2 F20, FEI, Hillsboro, OR, USA).

2.3. Creep Test and Characterization

To reveal the influence of oxygen content on the creep property of FGH96 superalloy, the creep experiment at 700 °C under 690 MPa was carried out on an electronic creep testing machine (RDL100, SINOTEST, Changchun, China). The drawing of the creep sample is illustrated in Figure 2. For the test of accuracy, two samples of each oxygen content were applied.

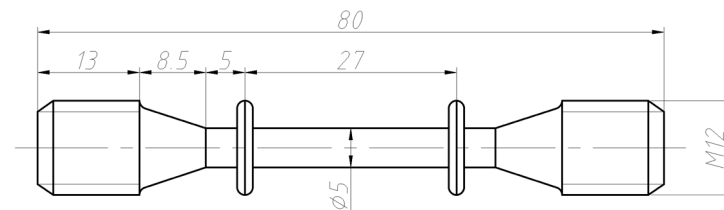


Figure 2. Drawing of creep sample.

The fracture morphology was observed by SEM under secondary electron (SE) mode, and the local misorientation maps before and after the creep experiments were obtained by SEM under EBSD mode. The annealing twin before and after creep experiment were also analyzed with TEM.

3. Results and Discussion

3.1. Effect of Oxygen Content on Microstructure of FGH96 Superalloy

Figure 3 shows the mechanically polished morphology of FGH96 superalloy with different oxygen content, indicating a clear spherical original powder particle boundary. According to the PPB grade evaluation principle given by Ingesten et al. [16], the PPB grades of FGH96 superalloy with oxygen content of 135 ppm and 341 ppm are grade 2 and grade 3, respectively, which means the higher the oxygen content, the more continuous the PPB will be.

The phase composition of FGH96 superalloy with different oxygen contents is mainly γ matrix, γ' phase and carbide. The γ' phase can be divided into three types: one is irregular long strips or large blocks (Figure 4a,b, marked γ'_1), which distributes at PPB; the second is petal-like or spherical (Figure 4c,d, marked γ'_2), which disperses inside the PPB; and the third is small spherical (Figure 4c,d, marked γ'_3), precipitating between γ'_2 phases. Quantitative metallography demonstrated the effect of oxygen content on γ' phase size, and the results are displayed in Table 2. It is clear that the oxygen content has a great influence on the γ'_1 phase size, which in the FGH96 superalloy with an oxygen content of 341 ppm increases by 20% compared with that of 135 ppm. Yet, the size of γ'_2 and

γ'_3 phases is rarely affected by oxygen content; the γ'_2 phase size of the superalloy with oxygen content of 135 ppm and 341 ppm is 325.4 nm and 320.7 nm, respectively, while the γ'_3 phase size is 22.6 nm and 24.8 nm, respectively.

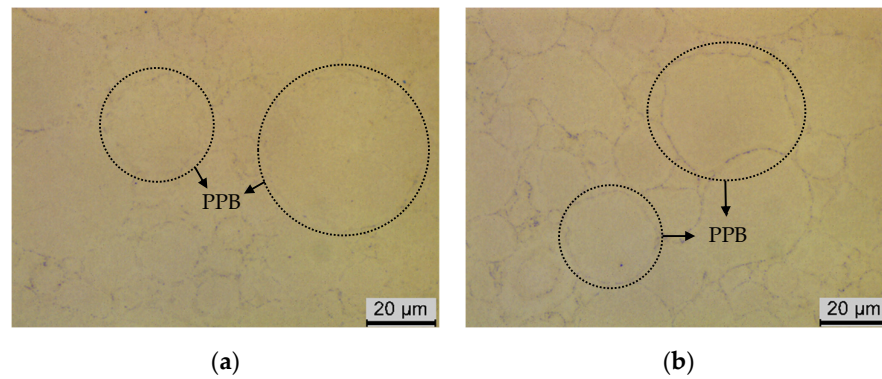


Figure 3. OM images of FGH96 superalloy with different oxygen content: (a) 135 ppm, (b) 341 ppm.

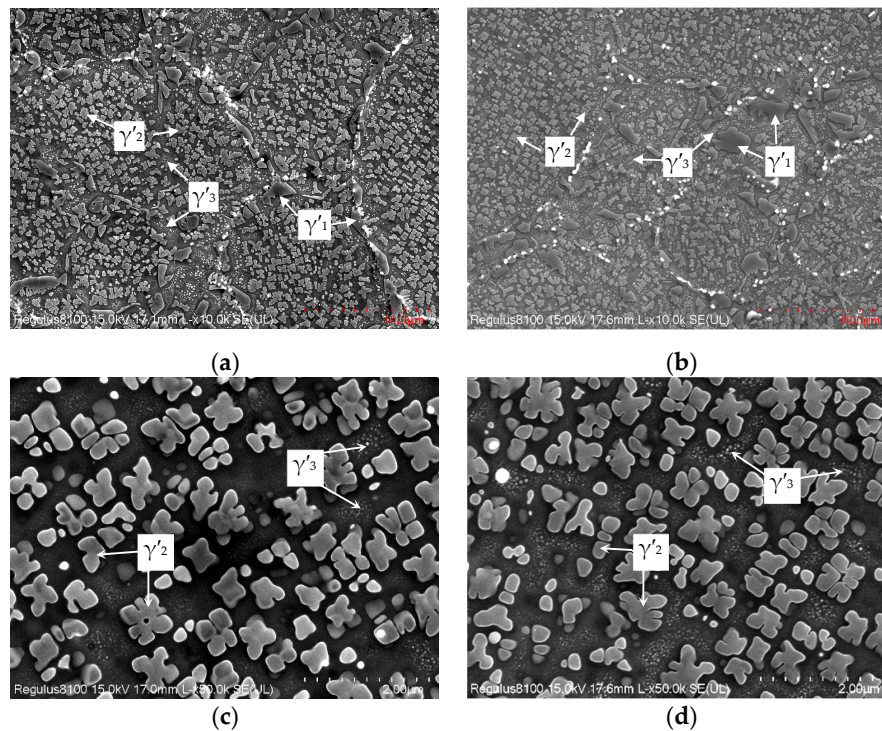


Figure 4. γ' phase morphology of FGH96 superalloy with different oxygen content: (a,c) 135 ppm, (b,d) 341 ppm.

Table 2. γ' phase size of FGH96 alloy with different oxygen content.

Oxygen Content/ppm	$\gamma'_1/\mu\text{m}$	γ'_2/nm	γ'_3/nm
135	1.07	325.4	22.6
341	1.27	320.7	24.8

From the SEM-BSE images in Figure 5a,b, carbide in FGH96 superalloy with different oxygen content has two forms: MC carbide with black contrast and $M_{23}C_6$ carbide with white contrast, both of which are scattered among PPB. Corresponding selected area electron diffraction patterns (SAED) are shown in Figure 5c,d, which are consistent with the results of reference [17,18]. The average size and percentage of these two kinds of carbides were statistically analyzed, and the results are displayed in Figure 6. When oxygen content

increases from 135 ppm to 341 ppm, the size of MC carbide increases from 77.4 nm to 104.1 nm and the percentage rises from 0.15% to 0.22%. Therefore, oxygen around the powder particle surface accelerates the precipitation and growth of MC carbide. However, oxygen content has little influence on the precipitation of $M_{23}C_6$ carbide. The average sizes of $M_{23}C_6$ carbide in FGH96 superalloy with oxygen contents of 135 ppm and 341 ppm are 768.9 nm and 824.3 nm, respectively, and the percentages are 0.10% and 0.11%, respectively.

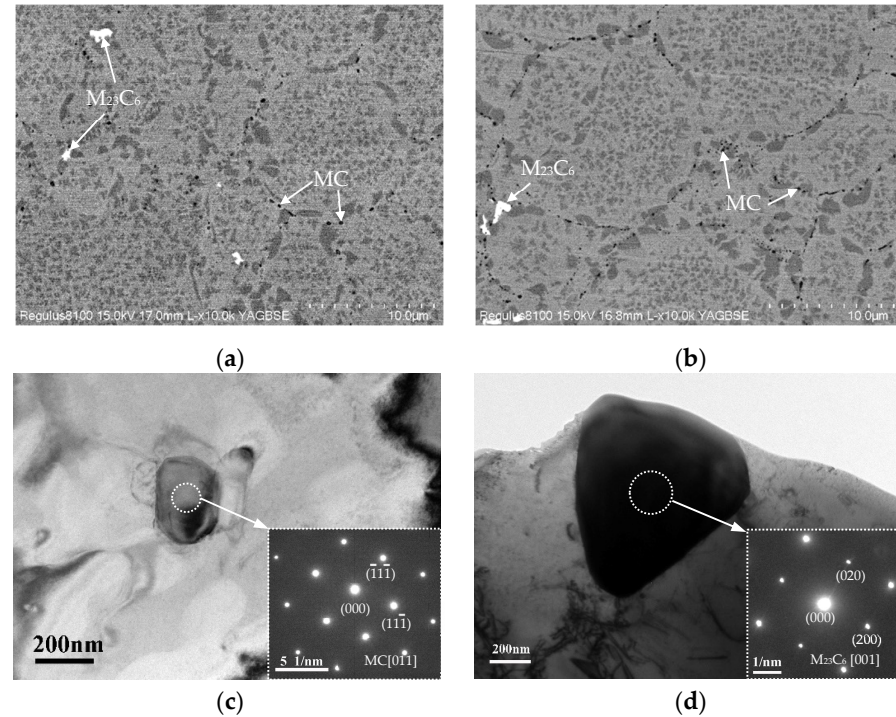


Figure 5. SEM-BSE images of FGH96 superalloy with (a) 135 ppm, (b) 341 ppm oxygen content and SAED patterns of (c) MC and (d) $M_{23}C_6$ carbides.

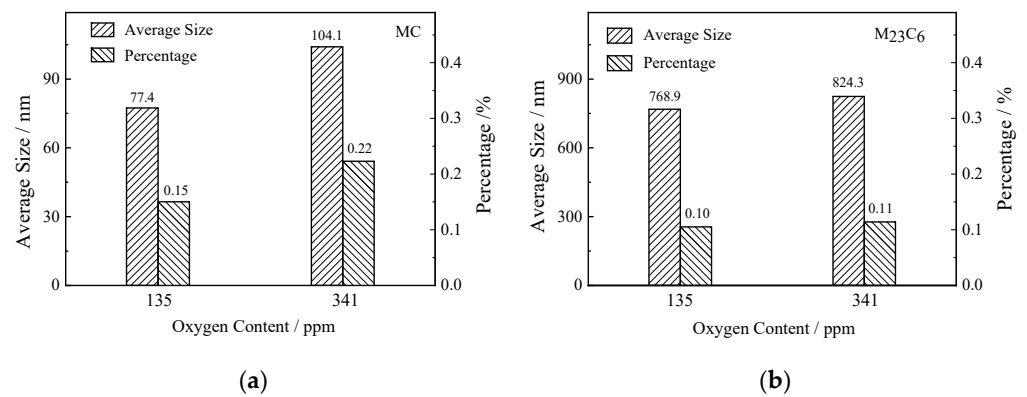


Figure 6. Histograms of carbide average size and percentage in FGH96 superalloy: (a) MC carbide, (b) $M_{23}C_6$ carbide.

In comparison with the original superalloy powder, Ni, Ti, Cr, Al, and other elements on the surface of the peroxidized powder oxidized more seriously, forming a thicker oxide layer as well as a broader alloy element deletion region [19]. In consequence, weaker driving force of γ' phase precipitation and mutual resistance of growing up around powder particle surface during HIPing result in bigger γ'_1 phase than γ'_2 phase and A larger average size of γ'_1 phase in FGH96 superalloy with higher oxygen content than that with lower oxygen content. Since the internal chemical state of the powder is nearly unaffected by surface oxidation, γ'_2 and γ'_3 phases in different oxygen content superalloys presented

almost the same morphology and average size. Meanwhile, a thicker oxide layer means more tiny oxide particles around the powder surface, tending to form more and bigger MC carbides at PPB.

The effect of oxygen content on crystal orientation and grain size distribution of FGH96 superalloy was studied by EBSD. Figure 7a,b illustrate the crystal orientation graphs of FGH96 superalloy with oxygen contents of 135 ppm and 341 ppm, respectively. Each crystal orientation is random, implying that the isotropous microstructure and oxygen content have no significant effect on the crystal orientation. But the grain size distribution changes significantly with the increase in oxygen content. According to the grain size distribution diagrams in Figure 8a,b, the maximum grain size of superalloy with an oxygen content of 341 ppm is 10 μm larger than that of 135 ppm, while the average grain size is smaller by 40%. Because the FGH96 superalloy with a higher oxygen content has more fine grains, mainly gathering around PPB, and the proportion of grains less than 2 μm is about 80% and 62%, respectively, and in the superalloy with an oxygen content of 341 ppm and 135 ppm, respectively. As a result, with the increase in oxygen content, the grain size distribution range becomes broader, but the average grain size is smaller.

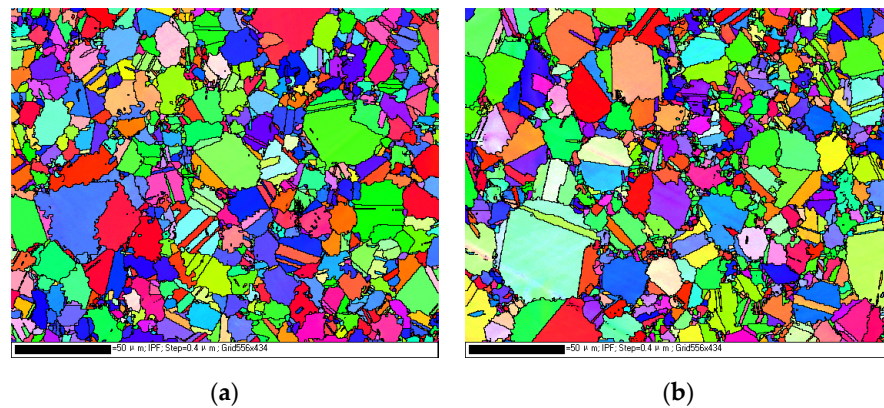


Figure 7. Crystal orientation images of FGH96 superalloy with different oxygen content: (a) 135 ppm, (b) 341 ppm.

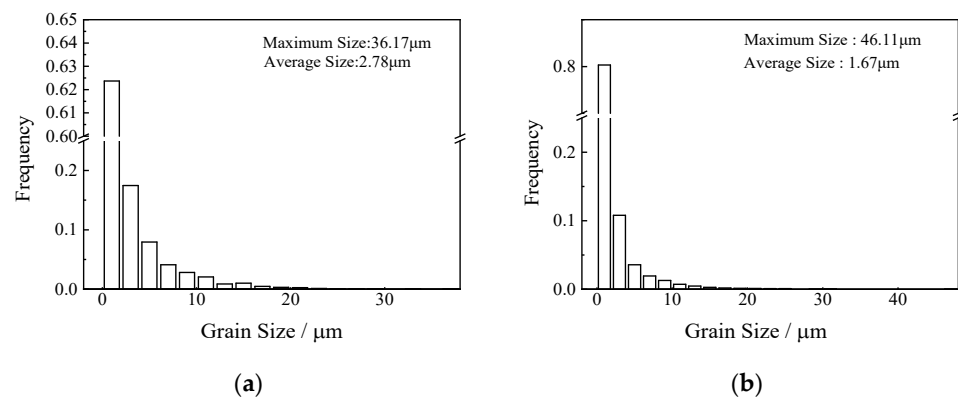


Figure 8. Grain size distribution of FGH96 superalloy with different oxygen content: (a) 135 ppm, (b) 341 ppm.

The grain size distribution has a strong relation to the degree of plastic deformation and recrystallization process during HIPing. The shear stress exerted by the external gas densifies the powder particles with drastic plastic deformation at the very beginning of HIPing. While the densified material tends to anneal in the following holding and cooling stages, the higher oxygen content of the powder tends to precipitate more oxides and carbides, which will hinder the deformation of the powder particles and grain growth [20]. Therefore, under the same HIPing condition, the powder with higher oxygen content

formed more continuous PPB, lowering the degree of plastic deformation, so the original large grain size of the powder was retained, and many fine recrystallization grains were also reserved owing to the insufficient driving force to grow up.

Figure 9 is the histogram of grain boundary distribution, and when the oxygen content increases from 135 ppm to 341 ppm, the twin boundary (60°), $\Sigma 3$, of the FGH96 alloy decreases from 34% to 30%, and the small angle boundary ($<10^\circ$) increases from 12% to 17%. Figure 10 shows the $\Sigma 3$ boundary distribution maps of superalloys with different oxygen contents. Similar to many FCC structure alloys, due to the low-level fault energy and large deformation during HIPing, a large number of annealing twins formed [21]. As described above, superalloys with a higher oxygen content deform harder during HIPing, and finely recrystallized grains are difficult to grow, so more small-angle grain boundaries are reserved.

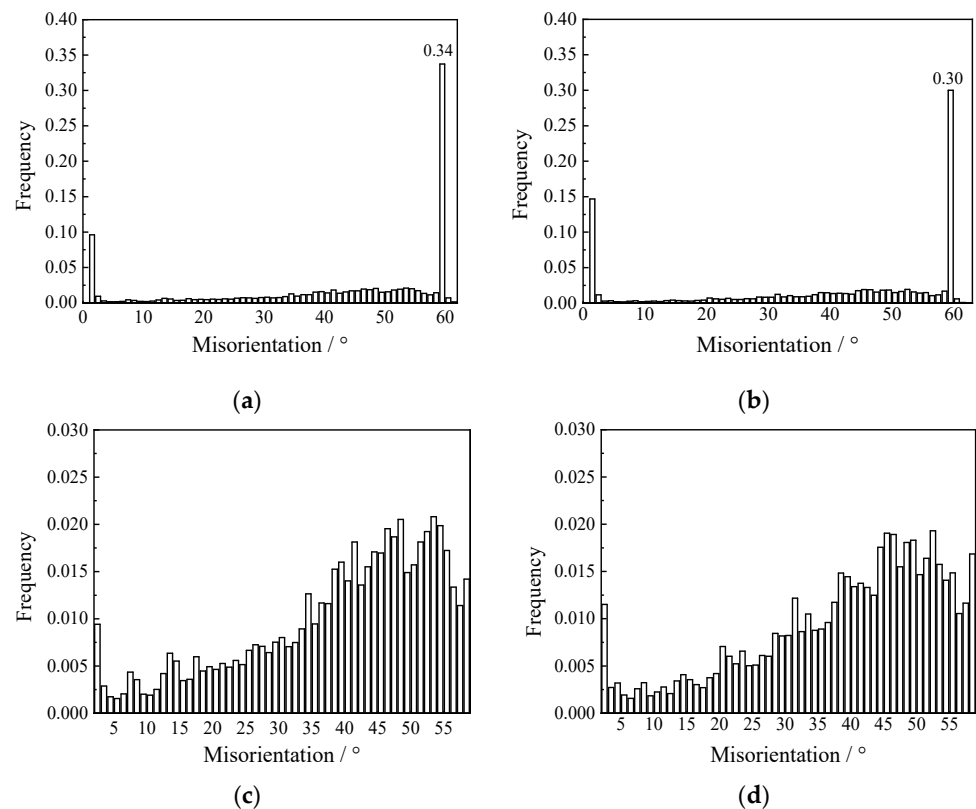


Figure 9. Grain boundary distribution of FGH96 superalloy with (a,c) 135 ppm, (b,d) 341 ppm oxygen content.

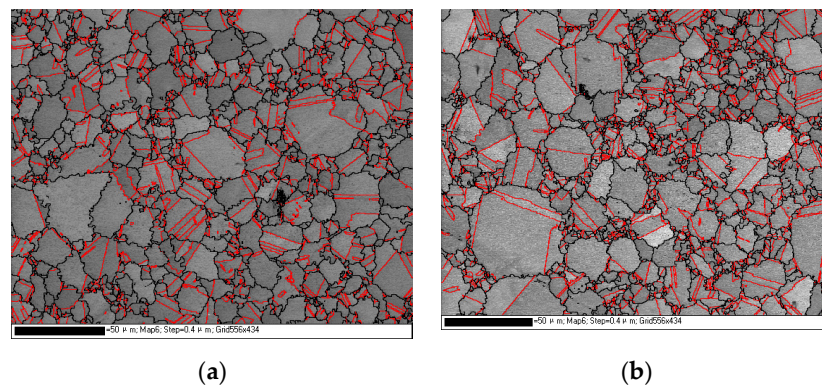


Figure 10. Twin boundaries of FGH96 superalloy with different oxygen content: (a) 135 ppm, (b) 341 ppm.

3.2. Effect of Oxygen Content on Creep Property of FGH96 Superalloy

The creep curves of FGH96 superalloy with different oxygen content at 700 °C and 690 MPa are displayed in Figure 11a. The two samples' creep curves for each oxygen content are almost the same, so one of the two samples in Figure 11b was chosen for analysis. The creep curves have three stages: the creep transition stage (I), the steady creep stage (II) and the creep acceleration stage (III). When the oxygen content increases from 135 ppm to 341 ppm, the duration of the steady creep stage decreases from 43 h to 21 h, the steady creep rate changes from $4.34 \times 10^{-3} \text{ h}^{-1}$ to $1.87 \times 10^{-2} \text{ h}^{-1}$, the creep life diminishes from 176 h to 94 h, and the total strain shortens from 13.9% to 8.5%.

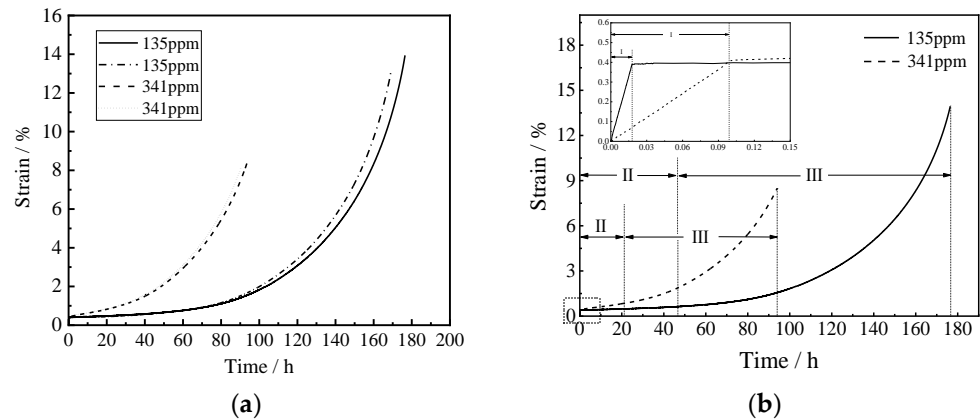


Figure 11. (a) Creep curves of FGH96 superalloy with different oxygen content and (b) creep curve of one sample of each oxygen content with enlarged area of the creep transition stage (I).

The creep fracture morphology of the sample with an oxygen content of 135 ppm contains three typical regions, namely the fracture source region, the crack extension region and the shear lip region, as shown in Figure 12a regions I, II and III, respectively. The crack originated at the edge of the sample, gradually expanded inward, and then tore rapidly. Figure 12b is the fracture source region, where a small number of PPB can be found. Wedge-shaped cracks can be seen from the enlarged image of the rectangular area in Figure 12b, indicating the intergranular and transgranular mixed fracture. Figure 12c displays the crack extension region, where there are a large number of deep dimples, implying a transgranular fracture feature, and a few PPB. Figure 12d is the shear lip region, in which a large number of shallow dimples exist.

The creep fracture morphology of the sample with an oxygen content of 341 ppm also has these three typical regions, as shown in Figure 13a: regions I, II and III, respectively. A large quantity of PPB appears in both the fracture source region and the crack extension region (Figure 13b,c), indicating that the crack originated at the PPB and also expanded along the PPB. No secondary cracks were found in the whole fracture, meaning that the crack extended quickly compared with the lower oxygen content creep sample, which confirms the creep curves. The shear lip region (Figure 12a region III) is relatively small compared with that of lower oxygen content (Figure 13a region III), and the shallow dimples can also be observed in Figure 13d.

The local misorientation distribution curves of the samples with different oxygen content before and after the creep experiment are demonstrated in Figure 14. There is no significant difference between the two local misorientation distribution curves before creep. However, after the creep test, the two local misorientation distribution curves dramatically changed, which indicates a large strain occurred in these two samples during the creep test. Compared with the creep sample with 341 ppm oxygen content, the sample with 135 ppm oxygen content has a broader local misorientation distribution, which means a larger strain during creep, and as a result, it has a longer creep life due to its lower crack extension rate.

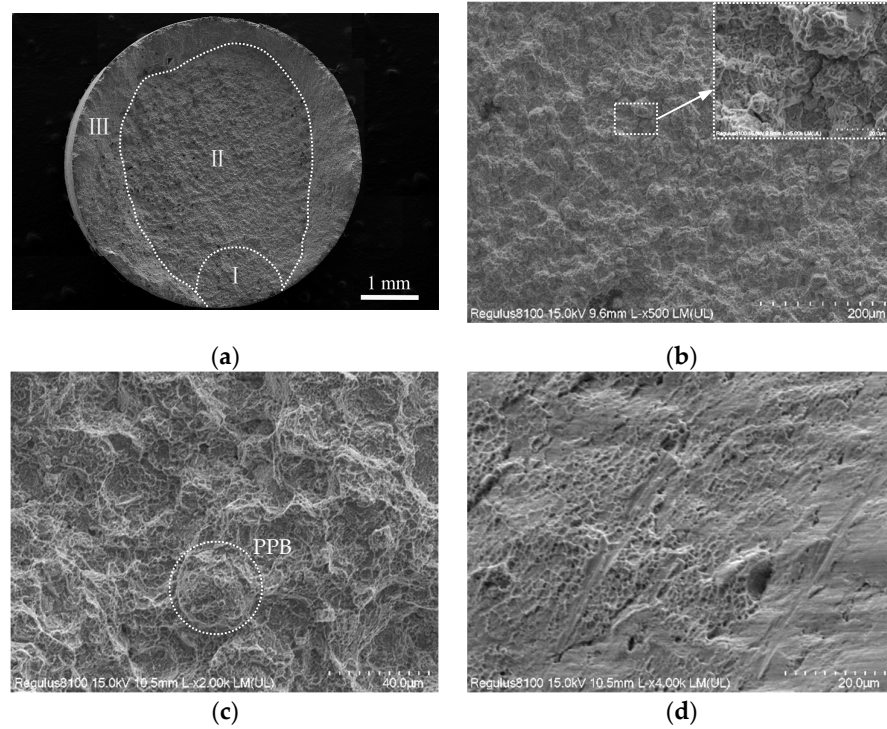


Figure 12. Creep fracture morphology sample with 135 ppm oxygen content: (a) overall fracture morphology, magnified image of region (b) I with enlarged area of wedge-shaped cracks, (c) II and (d) III in (a).

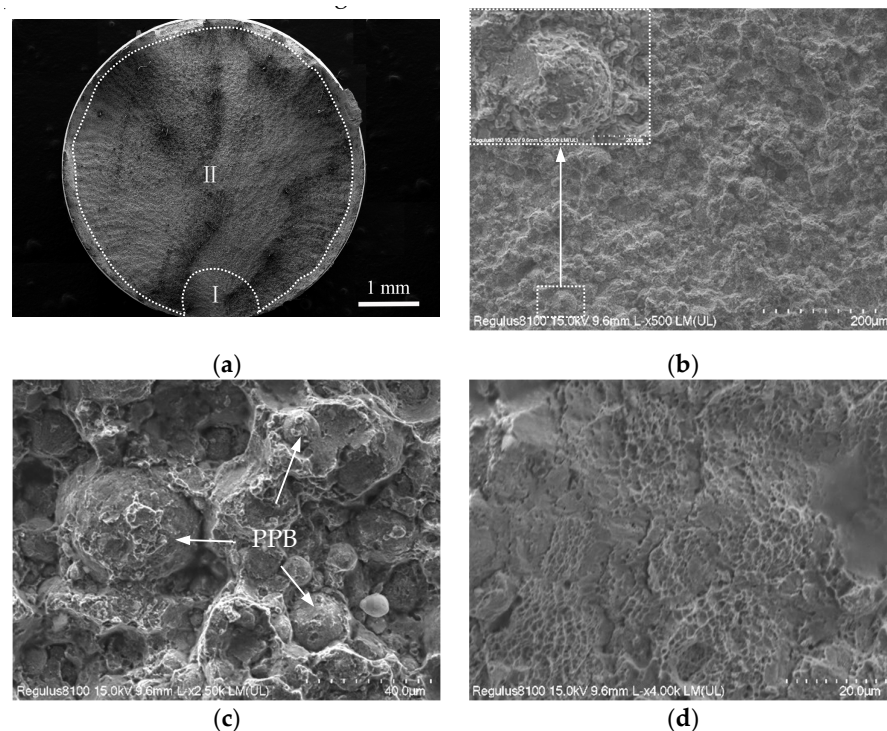


Figure 13. Creep fracture morphology sample with 341 ppm oxygen content: (a) overall fracture morphology, magnified image of region (b) I with enlarged area of PPB, (c) II and (d) III in (a).

The local misorientation maps of the samples with two different oxygen contents before and after the creep experiment are illustrated in Figure 15. Before the creep test, the two local misorientation maps exhibit uniform distribution. After the creep, the stain of the sample with an oxygen content of 135 ppm clusters on grain boundaries and in fine

grains, but the stain of the sample with an oxygen content of 341 ppm gathers around PPB. Therefore, when the oxygen content increases from 135 ppm to 341 ppm, the creep fracture changes from intergranular and transgranular mixed fracture to PPB fracture.

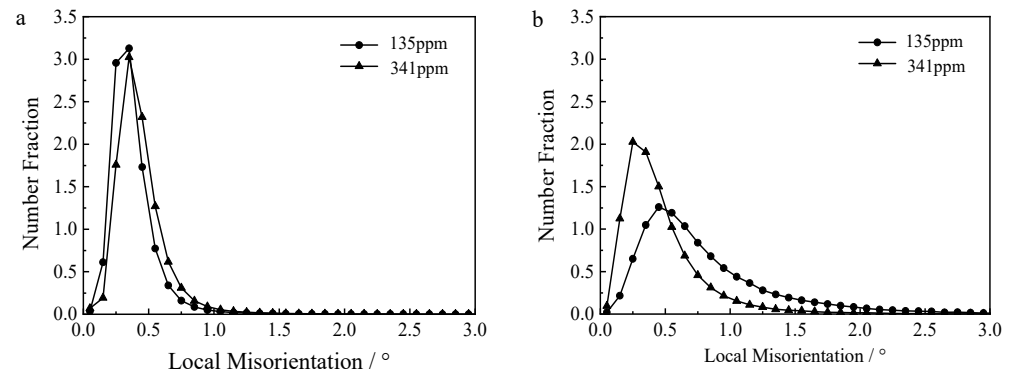


Figure 14. Local misorientation distribution: (a) before creep, (b) after creep.

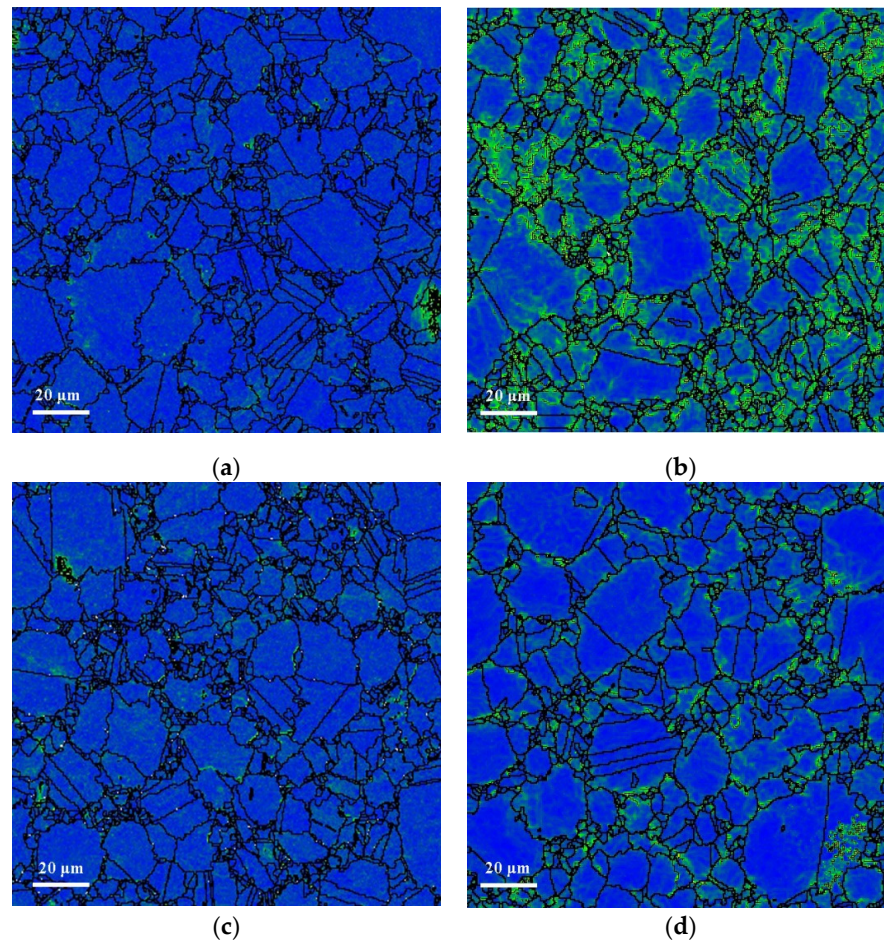


Figure 15. Local misorientation maps: (a) before creep with 135 ppm oxygen content, (b) after creep with 135 ppm oxygen content, (c) after creep with 135 ppm oxygen content, (d) after creep with 341 ppm oxygen content.

During creep, the sample releases stress concentrations through grain deformation and recrystallization. As analyzed above, deformation was resisted by the continuous PPB networks, and much finer recrystallization grains formed around PPB in FGH96 superalloy with an oxygen content of 341 ppm, thus the strain concentrated along PPB, becoming the crack origin and extension path.

3.3. Creep Mechanism

During the creep, dislocations form in the FCC-structured γ matrix and gradually slip to the γ - γ' phase interface, forming dislocation entanglement. The lattice mismatch stress between γ and γ' phases can be released by the dislocation entanglement, making dislocations cut through the γ' phase and forming two incomplete dislocations. One of the incomplete dislocations moves along the (111) crystal plane to form a stacking fault. Finally, micro-twins generate [22,23]. Figure 16a shows the micro-twin morphology of FGH96 superalloy with 135 ppm oxygen content, which are single-directional micro-twins. While Figure 16b displays two directional micro-twins in FGH96 superalloy with 341 ppm oxygen content, indicating the cross-slip phenomenon. Therefore, dislocation slip and micro-twin formation are the main creep deformation mechanisms of the FGH96 superalloy.

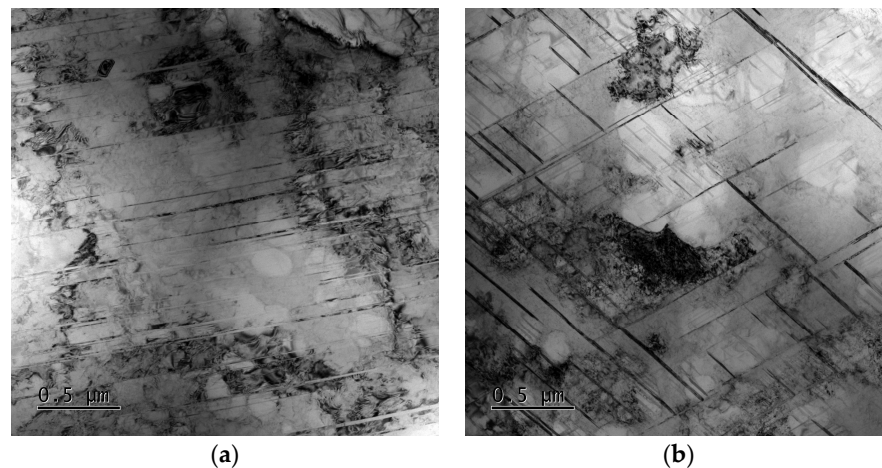


Figure 16. TEM images of samples after creep with different oxygen content: (a) 135 ppm, (b) 341 ppm.

However, the slip direction of the original $\Sigma 3$ boundaries in FGH96 superalloy differentiates these micro-twins, for which the micro-twin formation and movement will be limited. Consequently, the higher proportion of the $\Sigma 3$ boundaries in FGH96 superalloy with 135 ppm oxygen content slows down the creep rate and contributes to a longer creep life. While in FGH96 superalloy with 341 ppm oxygen content, multiple directions of the slip system motivate simultaneously and slip cross for the weaker resistance by $\Sigma 3$ boundaries, so the sample crept faster and ruptured earlier.

Therefore, necessary steps must be taken to control the oxygen content of the FGH96 superalloy. Firstly, the raw ingot must be remelted at high vacuum, and the molten alloy should be atomized by high-purity argon gas during powder making. Secondly, the powder needs to be protected by vacuum or inert gas when sieving and loading. Then, the loading container must be well sealed and densified at the proper parameters to prevent gas from leaking into.

4. Conclusions

The microstructure and creep properties of the FGH96 superalloy with different oxygen contents were investigated. The major findings are summarized as follows:

1. Oxygen content increased from 135 ppm to 341 ppm, PPB grade rose from grade 2 to grade 3, the size of the γ' phase on PPB enlarged from 1.07 μm to 1.27 μm , the MC carbide size grew from 77.4 nm to 104.0 nm and the MC volume fraction increased from 0.15% to 0.22%.
2. Oxygen content increased from 135 ppm to 341 ppm, steady creep duration shortened from 43 h to 21 h, and steady creep rate accelerated from $4.34 \times 10^{-3} \text{ h}^{-1}$ to $1.87 \times 10^{-2} \text{ h}^{-1}$, and creep rupture life decreased from 176 h to 94 h, and the creep rupture mode transferred from intergranular and trans-granular mixed fracture to along PPB fracture.

3. FGH96 superalloy with a 341 ppm oxygen content has a wider grain size distribution and fewer $\Sigma 3$ boundaries compared with lower oxygen content superalloys.
4. Multiple directions of slip system motivate simultaneously and slip cross for the weaker resistance by less $\Sigma 3$ boundaries in FGH96 superalloy with 341 ppm oxygen content, so the sample crept faster and ruptured earlier.

Author Contributions: Conceptualization, Z.L.; data curation, L.Z. (Lichong Zhang); funding acquisition, G.Z.; methodology, L.Z. (Lin Zhang); investigation and writing—original draft, Y.L. and S.Z.; writing—review and editing, L.Z. (Liang Zheng). All authors have read and agreed to the published version of the manuscript.

Funding: We are grateful for the financial support provided by the National Key Research and Development Program of China, grant number 2021YFB3704000, the National Nature Science Foundation of China, grant number 52071310) and the National Major Science and Technology Project of China, grant number Y2019-VII-0011-0151.

Data Availability Statement: Data are contained within the article.

Conflicts of Interest: The authors declare no conflict of interest.

References

1. Thuneman, T.; Raja, K.S.; Charit, I. Room Temperature Corrosion Behavior of Selective Laser Melting (SLM)-Processed Ni-Fe Superalloy (Inconel 718) in 3.5% NaCl Solution at Different pH Conditions: Role of Microstructures. *Crystals* **2024**, *14*, 89. [[CrossRef](#)]
2. Li, Y.; Zhang, Q.F.; You, X.G.; Qiang, J.B. Effect of Melt Superheating Treatment on the Microstructures and Purity of a Directionally Solidified Superalloy. *Crystals* **2023**, *13*, 1632. [[CrossRef](#)]
3. Tan, L.M.; He, G.A.; Liu, F.; Li, Y.P.; Jiang, L. Effects of Temperature and Pressure of Hot Isostatic Pressing on the Grain Structure of Powder Metallurgy Superalloy. *Materials* **2018**, *11*, 328–337. [[CrossRef](#)] [[PubMed](#)]
4. Qiu, C.L.; Attallah, M.M.; Wu, X.H.; Andrews, P. Influence of hot isostatic pressing temperature on microstructure and tensile properties of a nickel-based superalloy powder. *Mater. Sci. Eng. A* **2013**, *564*, 176–185. [[CrossRef](#)]
5. Ma, W.B.; Liu, G.Q.; Hu, B.F.; Jia, C. Formation of previous particle boundary of nickel base PM superalloy FGH96. *Acta Metall. Sin.* **2013**, *49*, 1248–1254. [[CrossRef](#)]
6. Zhou, J.Y.; Liu, C.K.; Zhao, W.X.; Zheng, Z.; Zhong, Y. Prior Particle Boundary of PM FGH96 Superalloy and Its In-situ High-cycle Fatigue at Elevated Temperature. *J. Aeron. Mater.* **2017**, *37*, 83–89.
7. Dong, K.X.; Yuan, C.; Gao, S. Oxidation Behavior of a Disk Powder Metallurgy Superalloy. *Mater. Sci. Forum* **2017**, *898*, 467–475. [[CrossRef](#)]
8. Yu, C.T.; Wang, Q.C.; Chen, M.H.; Wang, F.H. Microstructures and oxidation behavior of PM Ni-based superalloy FGH97 with in-situ carbide precipitates. *Corros. Sci.* **2023**, *220*, 111295. [[CrossRef](#)]
9. Liu, H.S.; Zhang, L.; He, X.B.; Qu, X.H.; Zhu, H.M.; Zhang, G.Q. Effect of oxygen content and heat treatment on carbide precipitation behavior in PM Ni-base superalloys. *Int. J. Min. Metall. Mater.* **2012**, *19*, 827–835. [[CrossRef](#)]
10. Zhang, Y.; Zhang, Y.W.; Sun, Z.K.; Huang, H. Influence of PPB on Fatigue Crack Growth Rate of PM Ni-Based Superalloy. *Rare Metal Mat. Eng.* **2019**, *48*, 3282–3288.
11. Rao, G.A.; Srinivas, M.; Satma, D.S. Effect of oxygen content of powder on microstructure and mechanical properties of hot isotatically pressed superalloy Inconel 718. *Mater. Sci. Eng. A* **2006**, *435*, 84–99. [[CrossRef](#)]
12. He, G.A.; Ding, H.H.; Liu, C.Z.; Liu, F.; Lan, H.; Jiang, L. Effects of powder characteristics on microstructure and deformation activation energy of nickel based superalloy. *Chin. J. Nonferrous Met.* **2016**, *26*, 37–49.
13. MacDonald, J.E.; Khan, R.H.U.; Aristizabal, M.; Essa, K.E.A.; Lunt, M.J.; Attallah, M.M. Influence of powder characteristics on the microstructure and mechanical properties of HIPed CM247LC Ni superalloy. *Mater. Des.* **2019**, *174*, 107796. [[CrossRef](#)]
14. Tian, T.; Hao, Z.B.; Ge, C.C.; Li, X.; Peng, S.; Jia, C. Effects of stress and temperature on creep behavior of a new third-generation powder metallurgy superalloy FGH100L. *Mater. Sci. Eng. A* **2020**, *776*, 139007. [[CrossRef](#)]
15. Peng, Z.C.; Liu, P.Y.; Wang, X.Q.; Luo, X.J.; Liu, J.; Zou, J.W. Creep Behavior of FGH96 Superalloy at Different Service Conditions. *Acta Metall. Sin.* **2022**, *58*, 673–682.
16. Ingesten, N.G.; Warren, R.; Winberg, L. *The Nature and Origin of Previous Particle Boundary Precipitates in P/M Superalloys*; Springer: Dordrecht, The Netherlands, 1982; pp. 1013–1027.
17. Liu, A.; Zhang, Y.T.; Wang, X.S.; Xu, W.; Zhang, Y.; He, Y.H. Evaluation of the influences of the stress ratio, temperatures, and local microstructure on small fatigue crack propagation behavior of the FGH96 superalloy. *Int. J. Fatigue* **2023**, *171*, 107573. [[CrossRef](#)]
18. Zhao, J.P. Study on Prior Particle Boundary (PPB) Precipitation in P/M Superalloy FGH96. Ph.D. Thesis, Xi'an University of Architecture and Technology, Xi'an, China, 2010.
19. Ning, Y.; Yao, Z.; Fu, M.W.; Guo, H. Recrystallization of the hot isostatic pressed nickel-base superalloy FGH4096: I. Microstructure and mechanism. *Mater. Sci. Eng. A* **2012**, *539*, 101–106. [[CrossRef](#)]

20. Sreenu, B.; Sarkar, R.; Kumar, S.S.S.; Chatterjee, S.; Rao, G.A. Microstructure and mechanical behaviour of an advanced powder metallurgy nickel base superalloy processed through hot isostatic pressing route for aerospace applications. *Mater. Sci. Eng. A* **2020**, *797*, 140254.
21. Peng, Z.C.; Zou, J.W.; Wang, X.Q. Microstructural characterization of dislocation movement during creep in powder metallurgy FGH96 superalloy. *Mater. Today Commun.* **2020**, *25*, 101361. [[CrossRef](#)]
22. Peng, Z.C.; Zou, J.W.; Yang, J.; Tian, G.F.; Wang, X.Q. Influence of γ' precipitate on deformation and fracture during creep in PM nickel-based superalloy. *Prog. Nat. Sci.* **2021**, *31*, 303–309. [[CrossRef](#)]
23. Peng, Z.C.; Zou, J.W.; Wang, Y.; Zhou, L.; Tang, Y. Effects of solution temperatures on creep resistance in a powder metallurgy nickel-based superalloy. *Mater. Today Commun.* **2021**, *28*, 102573. [[CrossRef](#)]

Disclaimer/Publisher's Note: The statements, opinions and data contained in all publications are solely those of the individual author(s) and contributor(s) and not of MDPI and/or the editor(s). MDPI and/or the editor(s) disclaim responsibility for any injury to people or property resulting from any ideas, methods, instructions or products referred to in the content.